Observations of Wave-induced Vortices over Ripples

Claire S. Nichols *

Abstract

Our understanding of vortex generation over rippled beds is largely based on small-scale laboratory studies. The insight provided by such studies has been considerable, although questions remain regarding the applicability to the field. This paper presents observations from a full-scale investigation of wave-induced vortex generation events over a movable sediment bed. Observations of the two-dimensional time varying velocity field were obtained with a submersible Particle Image Velocimetry (PIV) system in a field-scale, experimental environment at the O. H. Hinsdale Wave Research Laboratory. The observations were obtained over an irregularly rippled bed with ripple heights of 0.01 m and wavelength of roughly 0.1 m. The vortices generated during offshore directed flow over the steeper bed form slope were regularly ejected into the water column. The observations allowed for an examination of the generation and subsequent ejection of individual vortical structures. Vortical structures are identified with a measure of the flow field that estimates the time for a complete revolution of a vortice called swirling strength. An analysis of these structures reveals that the swirling strength non-dimensionalized by the wave period is correlated to the Keulegan-Carpenter. These results offer new insight into fluid sediment interaction over rippled beds.

*Graduate Student. The Ohio State University Department of Civil and Environmental Engineering and Geodetic Science. 470 Hitchcock Hall. 2070 Neil Ave. Columbus, OH 43210. Office: (614) 292-9582. Fax: (614) 292-3780. Email: nichols.236@osu.edu

1 Introduction

Investigations empirically relating vortex shedding over rippled beds to oscillatory flows date back to Darwin (1883) and Bagnold (1946). Through a series of empirical studies, these two pioneers suggested that vortices form on the lee side of ripples and are capable of suspending sediment if the hydrodynamic conditions remain within a limited window. Photographic and hot-wire observations by Nakato *et al.* (1977) and Honji *et al.* (1980) later confirmed the Darwin and Bagnold hypotheses. The investigations also showed vortices that separate from the bed are capable of advecting sediment (Honji *et al.*, 1980) and that this ejection occurs as the velocity passes through zero (Nakato *et al.*, 1977). Recently, more detailed observations of vortex shedding induced by oscillatory motions have been made in a series of small-scale laboratory experiments (e.g. Earnshaw and Greated (1998); Ahmed and Sato (2001); Sand Jespersen *et al.* (2004); Ourmieres and Chaplin (2004)). Most of these observations were obtained over fixed beds in laminar or transitionally-turbulent flow (see Table 1 for a summary of the experimental parameters). These observations have provided considerable detail and insight; however, questions remain regarding the applicability of these small-scale observations to fully-turbulent flow at field scale.

Field-scale observations of fluid-sediment interactions over rippled beds have primarily been limited to one-dimensional profiles of the water column, (e.g. Osborne and Vincent (1996), Thorne and Hanes (2002), Smyth *et al.* (2002), Chang and Hanes (2004), Foster *et al.* (2007)). These observations have shown significantly different wave bottom boundary layer characteristics for a range of bed geometries. For example, Smyth *et al.* (2002) observed that irregular ripples exhibit the largest magnitudes of nearbed turbulence, reinforcing the idea that vortex shedding may play a

significant role in the wave bottom boundary layer dynamics.

The objective of this effort is to provide evidence of vortex generation and ejection over movable rippled beds in a full-scale, free surface wave environment. Field-scale laboratory observations of the lowest 0.23 m of the water column are obtained with new particle image velocimetry (PIV) observations. The PIV technique uses the motion of seed particles visualized in image sets to calculate velocity fields. While PIV has been used extensively in controlled lab environments (e.g. Adrian (1991), Willert and Gharib (1991), Rockwell *et al.* (1993), Adrian (2005)), it has only recently been deployed in the ocean environment (e.g. Nimmo Smith *et al.* (2002), Nimmo Smith *et al.* (2004)). In the nearshore, such observations are complicated by the dynamic nature of the bed, unpredictable optical quality of the water, and generally harsh wave environment. These observations are the first full-scale observations of the two-dimensional time-varying flow field dynamics over movable rippled beds.

2 Observations

The observations for this effort were obtained during the summer of 2005 as part of the collaborative, multi-institutional CROss Shore Sediment Transport EXperiment (CROSSTEX). The experiment was performed in the Large Wave Flume (LWF) at the O. H. Hinsdale Wave Research Laboratory at Oregon State University. The LWF is 104 m long, 3.7 m wide, and 4.6 m deep, with a programmable, hinged-type hydraulic ram wave generator capable of producing oscillatory flows and simulating regular, as well as random, wave groups. The offshore wave conditions in this study were defined with a TMA spectrum specified with a significant wave height (H_{mo}), wave period (T), and spectrum spread (γ) of 0.4 m, 6 s, and 10, respectively. At approximately 30 m

offshore, with a still water depth of 1.6 m, this resulted in a root-mean-square horizontal velocity, u_{RMS}, of 0.24 m/s and a mean horizontal velocity, u_{mean}, of -0.3 m/s at an elevation of 0.6 m from the bed. Positive velocity is directed in the onshore and upward directions. The median grain size at the sampling location was 0.2 mm.

Five independent, 48-second PIV realizations were obtained within a 7.5 minute duration of the 20-minute wave run (Table 2). An Acoustic Doppler Velocimeter (ADV) sampled the free stream velocity at 25 Hz at an elevation of 0.62 m from the bed (Figure 1). Observations of the two-dimensional (x-z) flow field and bed geometry were obtained with a submersible Dantec PIV system. A 120 mJ Nd:Yag laser was located 0.7 m above the bed and illuminated a vertical (x-z) slice of the water column (Figure 1). An obliquely oriented 1 mega-pixel digital camera secured to the flume wall obtained 48-second bursts of image pairs over a 0.23 m x 0.23 m approximate area (x-z) of interest. Image pairs were collected at a 15 Hz sampling rate with a 3 ms temporal lag between image pair members. Seeding material included natural organic material as well as entrained sediment. Two-dimensional velocity fields were calculated with adaptive correlations of 32 x 32 pixel windows with a 50% overlap in a manner consistent with Nimmo Smith *et al.* (2004). At a velocity of 0.50 m/s, particles will travel 2 mm or approximately 25% of the interrogation window. This give a resolution of 0.2 mm/pixel Unresolved velocity vectors result from one of the following three situations: 1) when the number of scatters is too low; 2) when the nearbed sediment concentration is too large or there is a large reflection from the bed; and 3) in the low-illumination part of the image that is focused on the bed between the laser plane and the camera.

3 Results

The mean bed elevation over each of the five, 48-second realizations was assumed to be the centroid of the light reflected from the bed of the mean image (see Figure 2 for an example of the mean image for the second realization). The region of the image below the high intensity bed reflection is the water-sediment interface located between the laser sheet and the camera. This region is outside the plane of the laser sheet and consequently the correlations are low and all velocity estimates are neglected. The upper and lower bounds of the bed reflection were defined as the elevation at 95% of the maximum light intensity. These values were less than 6 mm from the mean bed elevation (Figure 2(a)). Over the course of the five realizations, the bedform maintained its general shape with a wavelength, λ_b, of roughly 0.1 m and ripple height, η_b ranging from 0.01 to 0.015 m, but migrated onshore at a rate varying from 0.0001 to 0.0005 m/s (0.01 to 0.05 cm/s). Table 2 gives bedform migration rates for individual realizations.

Figure 2 also shows the root-mean-square (RMS) flow field calculated for all valid vectors over the second realization. There exists a relatively small boundary layer thickness that varies over the bedform. The boundary layer shows its thickest profile, 0.025 m, in the deepest bedform trough at x = 0.03 m. The observed wave bottom boundary layer thickness compares favorably to that of a 0.027 m layer thickness predicted only considering the grain roughness ($k_s = 2.5d_{50}$) by the Madsen (1994) empirical model that is derived from the Grant and Madsen (1979) eddy viscosity formulation. However, if the roughness is parameterized with the ripple geometry ($k_s = 27.7\eta_b^2/\lambda_b$) (Grant and Madsen, 1982), the predicted wave bottom boundary layer thickness of 0.05 to 0.07 m (depending on the ripple height assumed) is significantly larger than the observations. An

examination of the non-negligible root-mean-square velocities near the sediment-water interface offers a potential explanation for this disagreement. At the ripple crests, the RMS velocity at the approximate bed location is as large as 0.2 m/s and would clearly not satisfy a no-slip boundary condition as is generally assumed. These seemingly large velocity estimates may result from poor correlations at the actual water-sediment interface where there is a large light reflection. However, they are not inconsistent with the Duck94 field observations of Foster *et al.* (2000) and Foster *et al.* (2006). The Duck94 observations consisted of a vertical array of hot films placed the wave bottom boundary layer and intermittently mobile sediment bed. The root-mean-square velocities at the bed ranged from 0.07 to 0.27 m/s under 5 s waves with a 0.35 m/s root-mean-square free stream wave velocity. These results also suggest that approximations of the wave bottom boundary dissipation, based on estimates of the shear velocity, u_*, would significantly over-predict the dissipation within the water column.

A cross spectral analysis between the horizontal velocity as measured with the ADV (z = 0.6 m), U_{ADV}, and as measured with the PIV system at the center uppermost PIV vector (x = 0.11 m, z = 0.23 m), U_{PIV}, shows strong coherence that exceeds the 95% significance level at frequencies below 0.7 Hz (Figure 3(b)). Beyond 0.7 Hz, the drop in coherence may result from the reasonably high noise floor of the ADV sensor evident in Figure 3(a). The two sensors are less than 10° out of phase at frequencies below 0.7 Hz (Figure 3(c)). A sample time series of U_{ADV} and U_{PIV} for the second realization is presented in the top panel of Figure 4. Following Cowen *et al.* (2003) and Efron and Tibshirani (1993), a bootstrap uncertainty interval at the 95% confidence level was determined for the random component for the uncertainty for the horizontal component of velocity.

In these calculations, the ADV is assumed to be the true value of the free stream velocity. Because of a reasonably high noise floor (see Figure 3), the ADV signal was low-pass band filtered at 1 Hz (with a 40 point taper). Interpolation of these structures is also limited because the U_{ADV} and U_{PIV} were vertically offset by 0.42 m. The 95% uncertainty interval for the second realization was found to be $\pm$ 0.098 m ($\pm 9\%$ of the peak velocity). The mean correlation coefficient of the bootstrap analysis for the second realization was 0.99 $\pm$ 0.13 (see Table 2 for the uncertainty for each realization).

Figure 4 shows the flow field and image evolution through an offshore directed flow excursion. The sequence consists of velocity vectors and the image of the peak offshore flow (Figure 4(a)), followed by flow deceleration (Figure 4(b)), and flow reversal (Figure 4(c)). In all cases the instantaneous velocity fields are mostly uniform above an elevation of 0.07 m from the reference elevation. The peak offshore velocity reaches 0.58 m/s over a 1/2 wave excursion of 2.8 seconds (Figure 4(a)-(c)). As the flow decelerates (Figure 4(b)), the nearbed flow at the steep slope of the most-offshore ripple (x = 0.05 m) separates and a vortex is formed. At this time, a sediment plume (shown by the higher intensity particles) is entrained into the structure. In the last panel (Figure 4(c)), the free stream velocity is zero and the phase lead of the wave bottom boundary layer is evident as the vortex and entrained sediment is released into the water column and advected with the flow.

Following Sveen (2004), the time-varying vorticity field are calculated with a least squares extrapolation. Unresolved velocity vectors are replaced with an 8 point weighted-average of the nearest neighbors. The vector field has been temporally smoothed with a 5-point running average

to reduce noise. An examination of the vorticity field for the offshore directed flow sequence in Figure 4 is shown in Figure 5. In this sequence, during the peak of the offshore excursion, there exists a region of high nearbed counter-clockwise-directed vorticity (Figure 5(a)). As the flow decelerates, the region of high vorticity is lifted into the water column (Figure 5(b)). Following ejection, the vortex is advected with the flow as it dissipates and loses its shape (Figure 5(c)).

In real fluids, the identification of such structures is complicated by diffusion and, in this case, boundary generated shear. Characterization is also complicated as random waves over movable rippled beds cannot easily be reduced to wave phase and an average ripple steepness (i.e. η_b/λ_b). Vorticity magnitude has been widely used to identify coherent vortical structures. However, this may not always be satisfactory since vorticity does not identify vortex cores in shear flow, especially if the background shear is comparable to the vorticity magnitude within the vortex (Jeong and Hussain, 1995). Since a vortex core must exclude a wall, vorticity is not a suitable criterion for vortex identification in a boundary layer. In the following analysis, we characterize vortical structures with the swirling strength criterion defined by Zhou *et al.* (1999). This criteria is based on the imaginary component of the eigenvalue, λ, of the velocity gradient tensor ($\mathbf{D}$), defined as

$$\mathbf{D} = \begin{bmatrix} \frac{\partial u}{\partial x} & \frac{\partial u}{\partial z} \\ \frac{\partial w}{\partial x} & \frac{\partial w}{\partial z} \end{bmatrix}. \tag{1}$$

In two dimensions, the characteristic equation is given by

$$\lambda^2 + P\lambda + Q = 0 \tag{2}$$

where the first invariant P = -tr($\mathbf{D}$) becomes

$$P = -\left(\frac{\partial u}{\partial x} + \frac{\partial w}{\partial z}\right) \tag{3}$$

and the second invariant, $Q = \frac{1}{2}((P)^2 - tr((\mathbf{DD})^2))$. For incompressible flow, P = 0. Although generally small in this two-dimensional environment, P is retained to account for any mass entering and leaving the laser sheet in the alongshore plane. The swirling strength, $\lambda_{ci}(x, z, t)$, is defined as the complex component of the eigenvalue. This method allows for easier spatial averaging in order to find the areas with the largest swirling strength without considering the nearbed shear. Following Nichols and Foster (2007), a Monte Carlo simulation of the vorticity and swirling strength parameters for the coherent structures present in Figures 4(b) and 5(b) was performed to examine how the propagation of errors in the velocity field will affect these quantities. This simulation revealed little error propagation.

An examination of the swirling strength field for the offshore directed flow sequence in Figure 4 is shown in Figure 6. In this sequence, as the flow decelerates (Figure 6(a)), a region of high swirling strength is evident over the most-offshore ripple at the steep slope (x = 0.06 m). As the flow reverses (Figure 6(b)), the high swirling strength region lifts into the water column and offshore into the trough of the ripple. Finally, at flow reversal (Figure 6(c)) the high swirling strength region is advected and dissipates.

An advantage of the swirling strength characterization is that is allows for spatial averaging without the need to artificially eliminate the boundary shear. The temporal evolution of the swirling strength is examined as a function of elevation by defining the horizontally averaged swirling strength, λ_{ci_H}, with

$$\lambda_{ci_H}(z,t) = \frac{1}{x_2 - x_1} \int_{x_1}^{x_2} \lambda_{ci}(x,z,t)dx \tag{4}$$

where $x_1 = 0$ m and $x_2 = 0.23$ m. As this is a spatially averaged quantity, the magnitude will be

lower than the local peaks in the swirling strength. The horizontally averaged swirling strength for the second realization is shown in Figure 7. The large-magnitude signals present in the nearbed region (0.025 $< z <$ 0.04 m) are indicative of forming vortical structures. During the longer-duration excursions, λ_{ci_H} often increases in magnitude as the structure builds strength until the flow reverses (i.e. $10 < t <$ 12.5 s). In this realization, several nearbed vortex generations are followed by vertically sloping swirling strength at $z \geq 0.04$ m and is evidence of vortex ejection. This characterization suggests a vortex ejection from $12.5 < t <$ 15 s and is consistent with Figure 4.

An estimate of the temporal duration of vortex generation was manually identified by high swirling in the nearbed region (see blue lines in Figure 7). This approximation allows for the examination of the hydrodynamic-forcing conditions present during generation. The hydrodynamic forcing involved in the generation of the vortical structures is examined with estimates of the Reynolds number, Re, and Keulegan-Carpenter number, KC. Following Hara and Mei (1990) and Ourmieres and Chaplin (2004), Re is characterized with

$$Re = \frac{|u_o| u_o T_{1/2}}{2\pi\nu} \tag{5}$$

where u_o is the peak velocity within a single one-half wave and $T_{1/2}$ is twice the duration between each zero-crossing. KC is characterized with

$$KC = \frac{u_o T_{1/2}}{\eta} \tag{6}$$

where η is the ripple height. KC is proportional to the inverse of the Strouhal number. In these formulations, Re and KC are signed quantities allowing for the examination of vortex generation as a function of flow direction. Figure 7 shows the variability of $|Re|$ and $|KC|$ for the second

realization. In general, vortex generation is present for the larger $|Re|$ and $|KC|$. Not surprisingly, the duration of vortex generation (i.e. high swirling from $0.02 < z < 0.07$ m) is longer for the longer durations of offshore-directed flow than for the shorter duration of onshore-directed flow.

As discussed above, λ_{ci} also shows evidence of vortex ejection. The ejecting structures show an upward slope of non-negligible swirling that follows high swirling in the nearbed region ($0.03 < z < 0.04$ m) (see the red lines on Figure 7). Interestingly, the two events with the strongest ejection signal (t = 12.5 and 43 s) occur when the onshore velocity, following the half-wave period of vortex generation, is relatively small. The vertical velocity of the ejected structure is calculated as the slope of each red line. The ejection velocities vary from 0.02 to 0.05 m/s in the upward direction.

Figure 8 illustrates the strong dependence of vortex generation (defined dimensionally with $\lambda_{ci_{peak}}$ or nondimensionally with $\lambda_{ci_{peak}} T_{1/2}$) on the hydrodynamic forcing (defined dimensionally with u_o or u_o^2 or nondimensionally with $|KC|$ or $|Re|$). Figure 8(b) shows the strongest trend of $\lambda_{ci_{peak}} T_{1/2}$ with $|KC|$. Despite the non-symmetric bedform, both onshore and offshore directed flows show a trend with $|KC|$ (although the offshore directed events are larger). This trend is less obvious for $|Re|$ and would suggest a lower dependence on the wave velocity. According to Zhou *et al.* (1999), the time for a structure to complete a single revolution is $\frac{2\pi}{\lambda_{ci}}$. Vortices that complete a revolution in less than a half-wave duration would then require that $\lambda_{ci} T_{1/2} > 4\pi$. In Figure 8, $\lambda_{ci_{peak}}$ has been filtered through vertical averaging, therefore this critical limit should be lower.

4 Discussion

The relationship shown in Figure 8 is significant for several reasons. First, it suggests the presence or absence of vortex structures for a given bedform shape may be purely characterized with the free stream horizontal velocity realization. Intuition would suggest that an upper limit of KC and Re would exist. If these non-dimensional numbers are increased beyond that upper limit, then, at some point, the bed would flatten. Second, if sediment is entrained in the structures, as these observations suggest, then it may be possible to examine Re or KC dependence with the large range of suspended sediment vertical profile observations that currently exist.

Finally, it provides questions pertaining to how smaller laboratory experiments may or may not be translated to field scale environments. These studies often incorporate sinusoidal waves and symmetrical fixed ripples (Sand Jespersen *et al.* (2004), Earnshaw and Greated (1998)). In Sand Jespersen *et al.* (2004), a single symmetric ripple oscillated in otherwise still fluid showed vortex evolution over single wave periods. They showed peak circulation which occurs just prior to flow reversal (170°) and is generally consistent with vortex ejection during offshore flow shown in Figure 6(d)-(f). However, the two structures differ in that our observations show no evidence of the vortex bending over the ripple crest following flow reversal. Earnshaw and Greated (1998) also do not show evidence of the ejected vortice being advected down into the next trough. Our observations are consistent with the ejection mechanism identified in Earnshaw and Greated (1998). However, the velocities in our study are significantly larger and more quickly dissipate the vortices.

5 Conclusions

Observations of the two-dimensional flow field over a natural sand bed have been obtained in a full-scale random wave environment. The observations are obtained with a submersible PIV system. Two-dimensional velocity fields are estimated over a 0.23 x 0.23 m^2 area. Five 48-second realizations are used to examine vortex generation and ejection over a rippled bed. Over the course of the sampling period the bedform migrated between 0.0001 to 0.0005 m/s in the onshore direction. The observed boundary layer thickness over this mobile bed of roughly 0.025 m is consistent with the boundary layer thickness predicted by the semi-empirical model of Madsen (1994), if the roughness is parameterized with the grain roughness. However, if the roughness is parameterized with the rippled bed geometry, the model thickness prediction is considerably greater than the observed thickness.

The dynamics of vortex generations are characterized with the swirling strength model of Zhou *et al.* (1999). Contours of swirling strength are consistent with estimates of vorticity and allow for an identification of the generation and ejection of individual events. An examination of the swirling strength over consecutive one-half wave segments shows that higher swirling strength events occur with increasing KC.

Once a vortex has formed, the ejection of the vortex is a function of the fluid characteristics following generation. A mild deceleration allows a vortex to lift into the water column and be advected. However, a steep deceleration restricts the vertical advancement of a vortex causing it to dissipate and not be advected. These results also suggest that the vortex ejection may be dependent on the local bedform slope. In these observations, most of the vortex ejections occur as the flow

reverse direction to onshore-directed flow. This would suggest that sediment is lifted over the bedform crest and is consistent with onshore migration of the ripples. These observations suggest that the generation and ejection of vortex structures may be predictable functions of the free-stream hydrodynamics and ripple geometry.

6 Acknowledgments

This work was supported by the National Science Foundation (OCE-0351903, CTS-0348203). C. Nichols gratefully acknowledges her adviser Diane Foster and the O. H. Hinsdale Research Laboratory staff and students. Also, this work would not have been possible without assistance from the Ohio State University Coastal Sediment Processes Lab. A special thank you to Lili Yu for her statistical consulting.

References

Adrian, R. J. (1991). Particle-imaging techniques for experimental fluid mechanics. *Annu. Rev. Fluid Mech.*, 23:261–304.

Adrian, R. J. (2005). Twenty years of particle image velocimetry. *Exp. in Fluids*, 39:159–169.

Ahmed, A. S. M. and Sato, S. (2001). Investigation of bottom boundary layer dynamics of movable bed by using enhanced piv technique. *Coastal Engineering Journal*, 43(4):239–258.

Bagnold, R. A. (1946). Motion of waves in shallow water, interaction between waves and sand bottoms. *Proceedings of the Royal Society of London. Series A, Mathematical and Physical Sciences*, 187(1008):1–18.

Chang, Y. S. and Hanes, D. M. (2004). Suspended sediment and hydrodynamics above mildly sloped long wave ripples. *J. Geophys. Res.*, 109:1–16.

Cowen, E. A., Sou, I. M., Liu, P. L., and Raubenheimer, B. (2003). Particle image velocimetry measurements within a laboratory-generated swash zone. *J. Eng. Mech.*, 129(10):1119–1129.

Darwin, G. H. (1883). On the formation of ripple-mark in sand. *Proc. Royal Society of London*, 36:18–43.

Earnshaw, H. C. and Greated, C. A. (1998). Dynamics of ripple bed vortices. *Exp. in Fluids*, 25:265–275.

Efron, B. and Tibshirani, R. J. (1993). *An Introduction to the Bootstrap*. Chapman and Hall.

Foster, D. L., Beach, R. A., and Holman, R. A. (2000). Field observations of the wave bottom boundary layer. *J. Geophys. Res.*, 105(C8).

Foster, D. L., Bowen, A. J., and Holman, R. A. (2006). Field evidence of pressure gradient induced incipient motion. *J. Geophys. Res.*, 111(C05004):doi:10.1029/2004JC002863.

Foster, D. L., Natoo, P., Stanton, T. P., and Fredsøe (2007). The suspension of sediment from flat and megarippled beds: A pairing of models and observation. *Cont. Shelf Res.*, page in press.

Grant, W. D. and Madsen, O. (1979). Combined wave and current interaction with a rough bottom. *J. Geophys. Res.*, 84(C4):1797–1808.

Grant, W. D. and Madsen, O. (1982). Movable bed roughness in unsteady oscillatory flow. *J. Geophys. Res.*, 87(C1):469–481.

Hara, T. and Mei, C. C. (1990). Centrifugal instability of an oscillatory flow over periodic ripples. *J. Fluid Mech.*, 217:1–32.

Honji, H., Kaneko, A., and Matsunaga, N. (1980). Flows above oscillatory ripples. *Sedimentology*, 27:225–229.

Jeong, J. and Hussain, F. (1995). On the identification of a vortex. *J. Fluid Mech.*, 285:69–94.

Madsen, O. (1994). Spectral wave-current bottom boundary layer flows. *Proc. Coast. Eng. 24th Intn'l Conf.*, 1:384–398.

Nakato, T., Locher, F. A., Glover, J. R., and Kennedy, J. F. (1977). Wave entrainment of sediment from rippled beds. *J. Waterw. Port, Coast. Ocean Eng.*, 103(WW1):83–99.

Nichols, C. and Foster, D. (2007). Full-scale observations of wave-induced vortex generation over a rippled bed. *J. Geophys. Res.*, page in press.

Nimmo Smith, W. A. M., Atsavapranee, P., Katz, J., and Osborn, T. R. (2002). Piv measurements in the bottom boundary layer of the coastal ocean. *Exp. in Fluids*, 33:962–971.

Nimmo Smith, W. A. M., Katz, J., and Osborn, T. R. (2004). On the structure of turbulence in the bottom boundary layer of the coastal ocean. *J. Phys. Oceanography*, 35:72–92.

Osborne, P. D. and Vincent, C. E. (1996). Vertical and horizontal structure in suspended sand concentrations and wave-induced fluxes over bedforms. *Marine Geology*, 131:195–208.

Ourmieres, Y. and Chaplin, J. R. (2004). Visualizations of the disturbed-laminar wave-induced flow above a rippled bed. *Exp. in Fluids*, 36:908–918.

Rockwell, D., Magness, C., and Towfighi, J. (1993). High image-density particle image velocimetry using laser scanning techniques. *Exp. in Fluids*, 14(3):181–192.

Sand Jespersen, T., Thomassen, J. Q., Andersen, A., and Bohr, T. (2004). Vortex dynamics around a solid ripple in an oscillatory flow. *Eur. Phys. J.*, 38:127–138.

Smyth, C., Hay, A. E., and Zedel, L. (2002). Coherent doppler profiler measurements of near-bed suspended sediment fluxes and the influence of bed forms. *J. Geophys. Res.*, 107(C8):1–20.

Sveen, J. K. (August 2004). *An introduction to MatPIV 1.6.1*. Department of Mathematics, University of Oslo, eprint no. 2 edition.

Thorne, P. D. and Hanes, D. M. (2002). A review of acoustic measurement of small-scale sediment processes. *Continental Shelf Res.*, 22:603–632.

Willert, C. E. and Gharib, M. (1991). Digital particle image velocimetry. *Exp. in Fluids*, 10:181–193.

Zhou, J., Adrian, R. J., Balachandar, S., and Kendall, T. M. (1999). Mechanisms for generating coherent packets of hairpin vortices in channel flow. *J. Fluid Mech.*, 387:353–396.

$Paper$	U_{max} (m/s)	T (s)	Re $\times 10^4$	KC	$Laboratory\ Setup$	d_{50} (mm)	η_b (m)	λ_b (m)
Jespersen et al. 2004	0.079, 0.145	2	0.22, 0.75	3.16	rigid lid sinusoidal	N/A	0.05	0.10
Ourmieres and Chaplin 2004	–	1-3.14	0.2 - 1.0	–	free surface sinusoidal	N/A	0.002, 0.004, 0.0048, 0.009	0.04, 0.05
Ahmed Sato 2001	0.48	3	12	72	rigid lid asymmetric	0.2	0.02	0.16
Earnshaw and Greated 1998 (a)	0.13, 0.20, 0.294	8.46	2.3, 5.4 11	31, 48 71	rigid lid sinusoidal	N/A	0.035	0.22
Earnshaw and Greated 1998 (b)	0.28	2.5	3.5	20	free surface sinusoidal	N/A	0.035	0.22
Current Effort 2006	1.1	6	≤ 60	456	free surface random	0.2	0.01	0.1

Table 1: Summary of previous and current experimental parameters.

$Realization$	t_{start} (sec)	t_{end} (sec)	$U_{rms_{PIV}}$ (m/s)	$U_{rms_{ADV}}$ (m/s)	R^2	$Migration\ Rate$ (m/s)	$U_{peak_{PIV}}$ (m/s)	$Uncertainty$ (m/s) (% of peak)
1	491	539	0.28	0.27	0.98	—-	0.91	$\pm$ 0.078 ($\pm 9\%$)
2	585	633	0.29	0.27	0.97	0.0005	1.07	$\pm$ 0.098 ($\pm 9\%$)
3	681	729	0.25	0.24	0.99	0.0001	0.82	$\pm$ 0.057 ($\pm 7\%$)
4	783	831	0.23	0.22	0.98	0.0003	0.91	$\pm$ 0.073 ($\pm 8\%$)
5	888	936	0.24	0.22	0.99	0.0003	1.04	$\pm$ 0.065 ($\pm 7\%$)

Table 2: Statistics for each of the realizations.

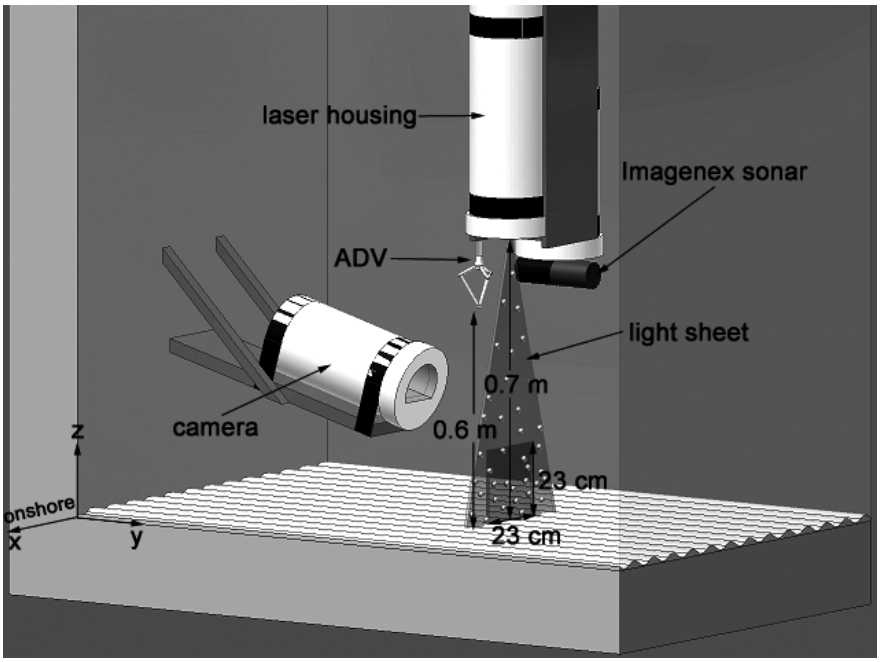

Figure 1: Schematic diagram of the submersible observation system.

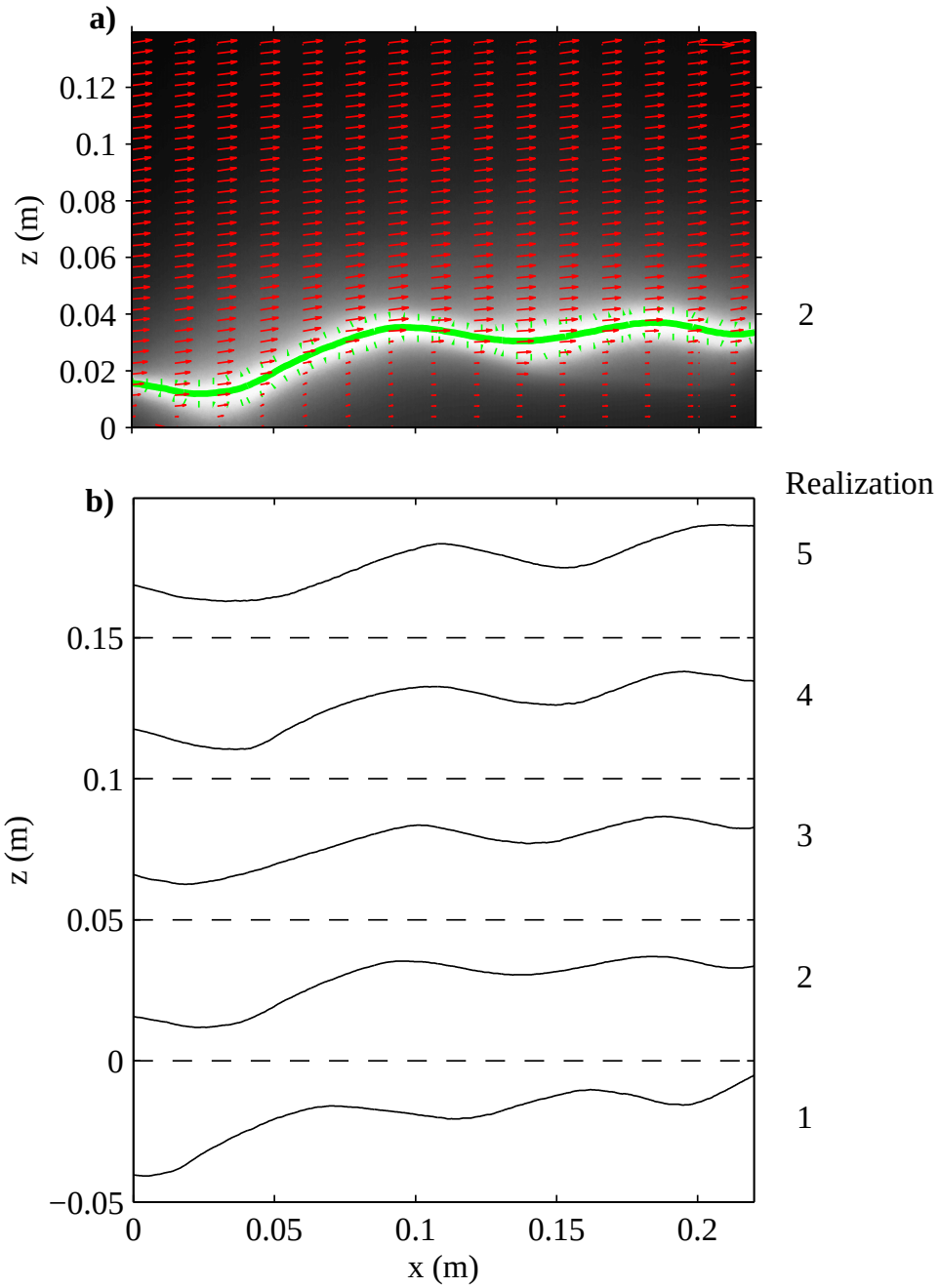

Figure 2: (a) The mean image intensity over the second 48-second PIV realization with the root-mean-square velocity field, u_{rms} (red vectors). The solid line shows the position of the centroid of the light reflected from the bed. The dotted lines show upper and lower bounds of the bed reflection. (b) The mean bed elevation for each of the 5 realizations. Each bed profile is vertically offset by 0.05 m. Onshore flow is directed to the right.

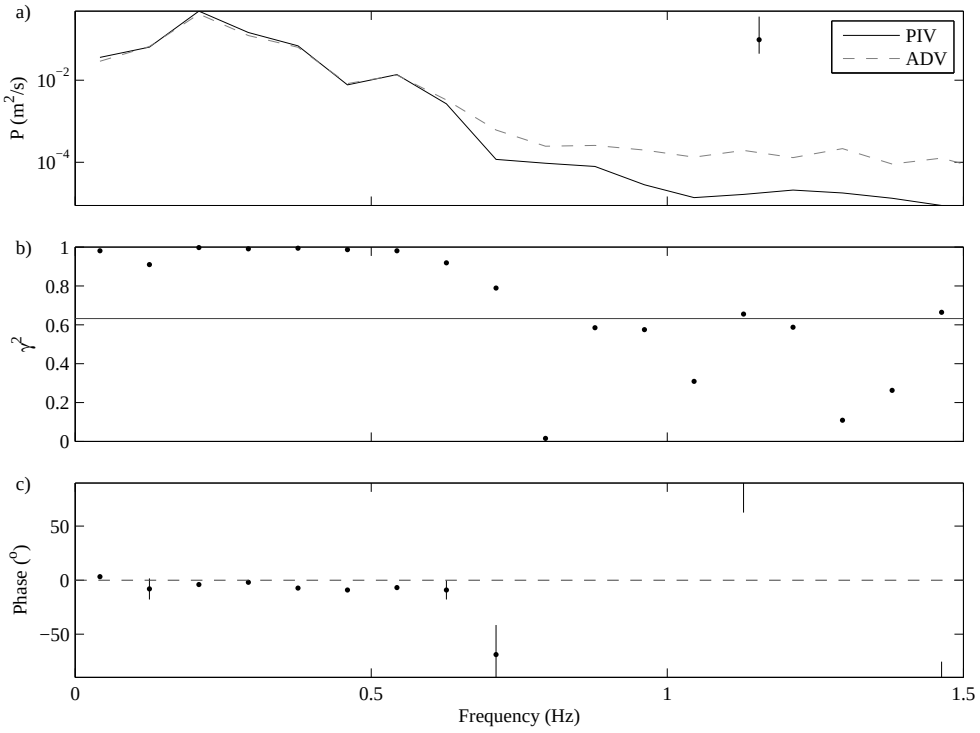

Figure 3: Horizontal velocity cross spectral analysis including the (a) power spectral density, (b) coherence, and (c) phase separation of U_{ADV} (dashed) and U_{PIV} (solid).

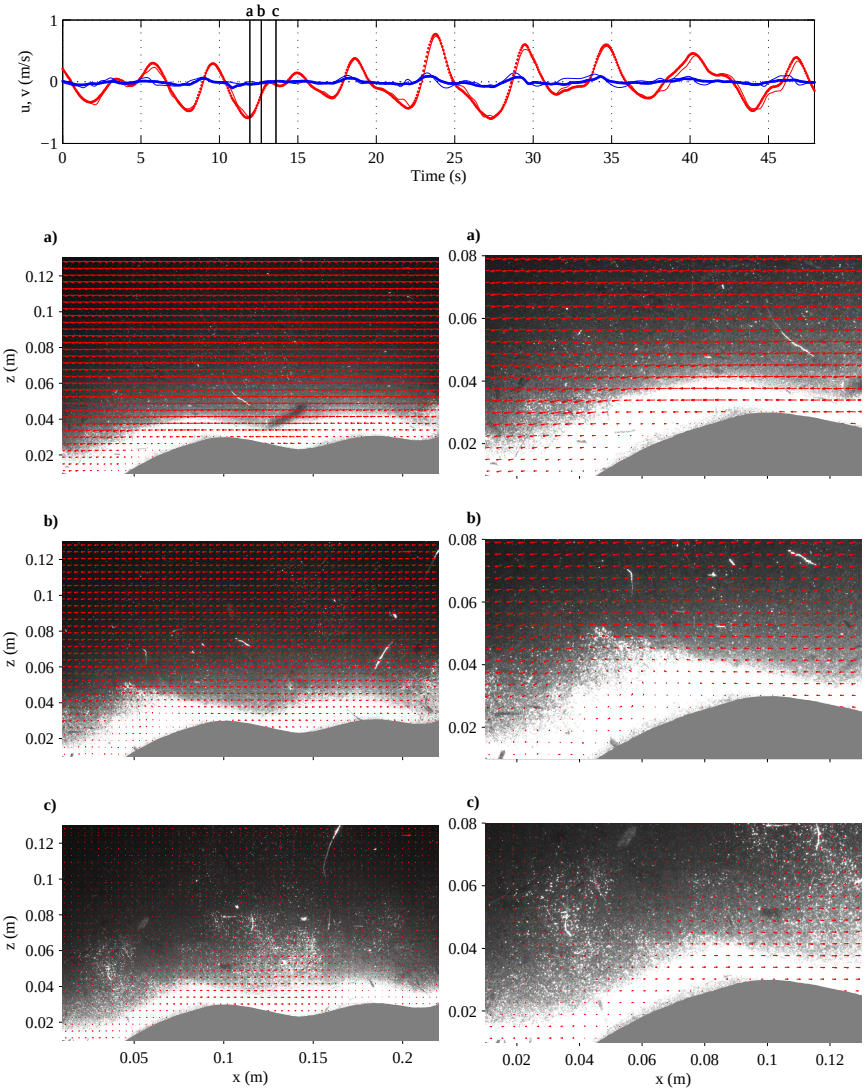

Figure 4: (Upper panel) A 48-second time series of horizontal (red) and vertical (blue) velocities as measured by the ADV (solid line) and PIV (dots) for the second realization. (a-c) Snapshots of the raw images and instantaneous velocity fields (red vectors) at the 3 times indicated in the time series in the upper panel. A 0.5 m/s scale vector is shown in the upper right of each image. The right panels are the same as the left panels, only a smaller area. Onshore flow is directed to the right.

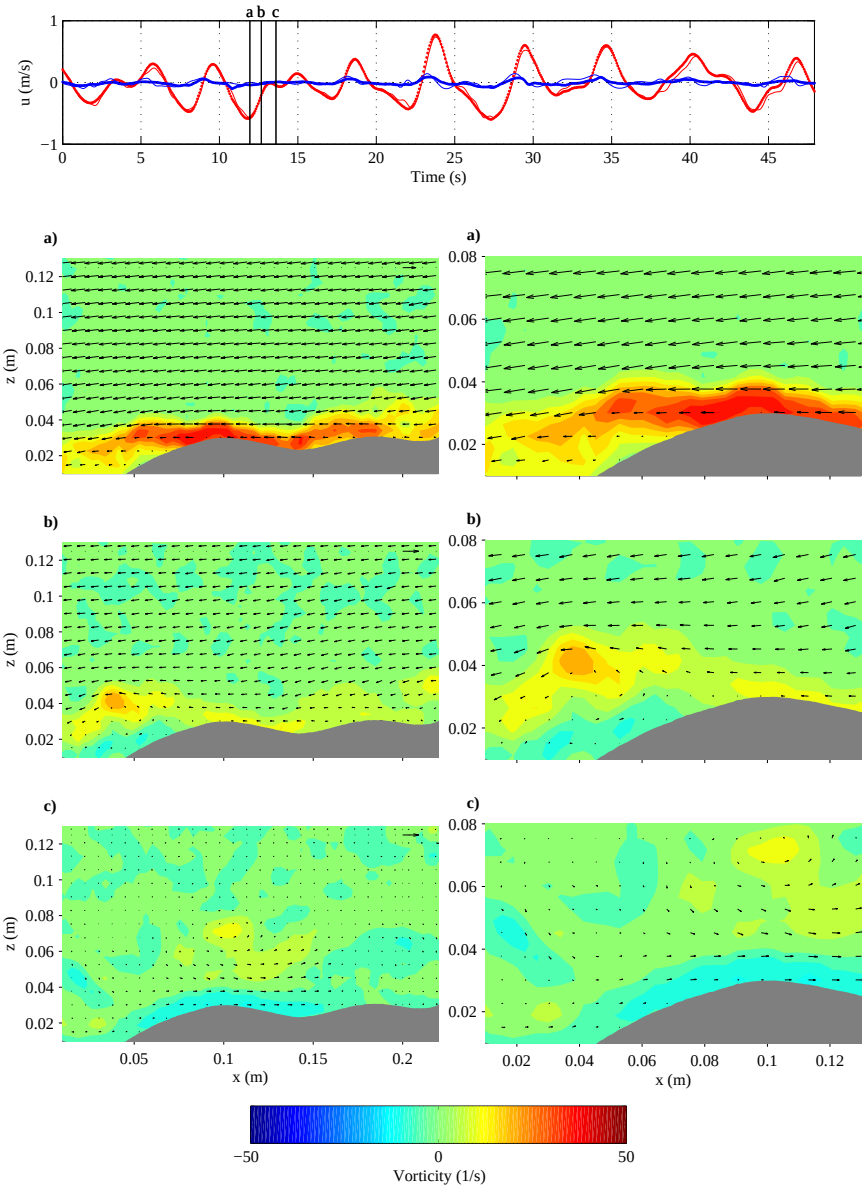

Figure 5: (upper panel) A 48-second time series of horizontal (red) and vertical (blue) velocities as measured by the ADV (solid line) and PIV (dots) for the second realization. (a-c) Snapshots of the vorticity field (color scale), 3 Hz low pass filtered velocity field (black vectors) at the 3 times indicated in the time series in the upper panel. A 0.5 m/s scale vector is shown in the upper right corner of each subfigure (black vector). The right panels are the same as the left panels, only a smaller area. Onshore flow is directed to the right. Positive vorticity represents flows rotating in the counter-clockwise direction

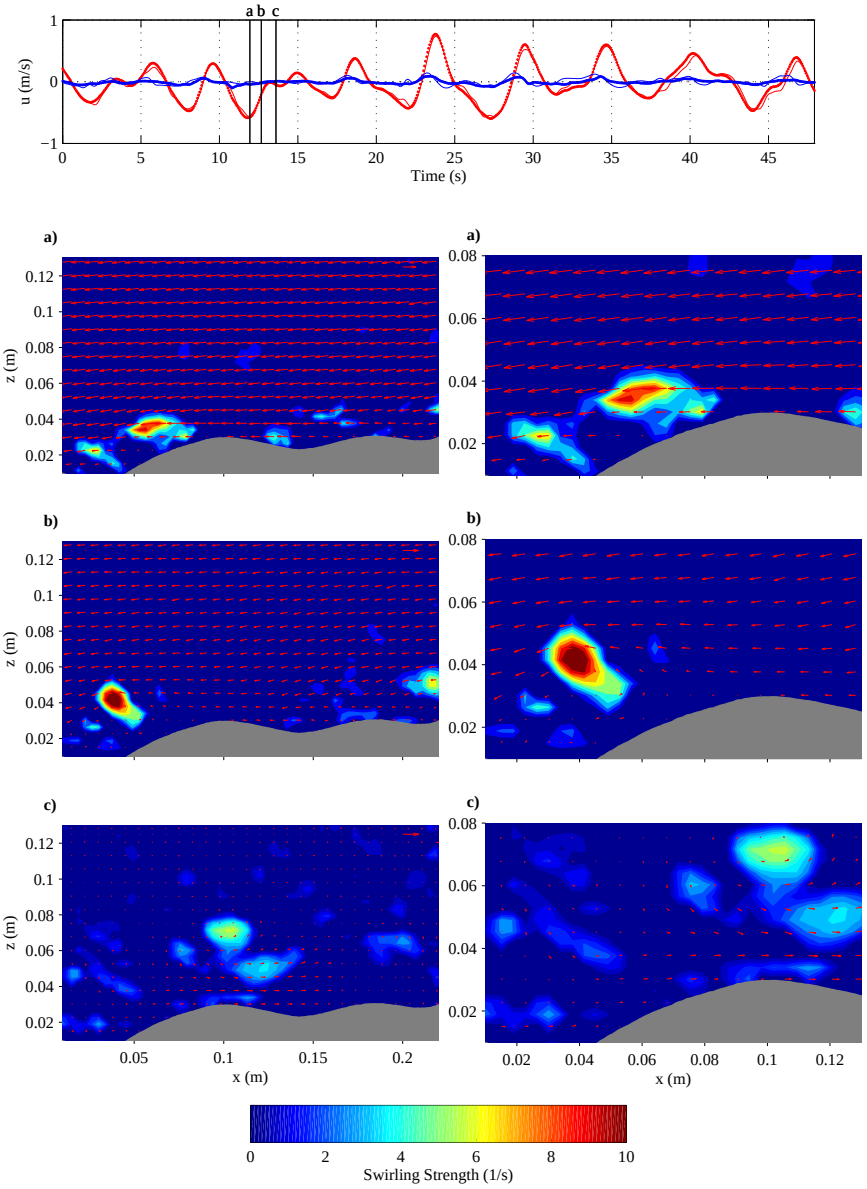

Figure 6: (upper panel) A 48-second time series of horizontal (red) and vertical (blue) velocities as measured by the ADV (solid line) and PIV (dots) for the second realization. (a-c) Snapshots of the swirling strength field (color scale), 3 Hz low pass filtered velocity field (red vectors) at the 3 times indicated in the time series in the upper panel. A 0.5 m/s scale vector is shown in the upper right corner of each subfigure (red vector). The right panels are the same as the left panels, only a smaller area. Onshore flow is directed to the right.

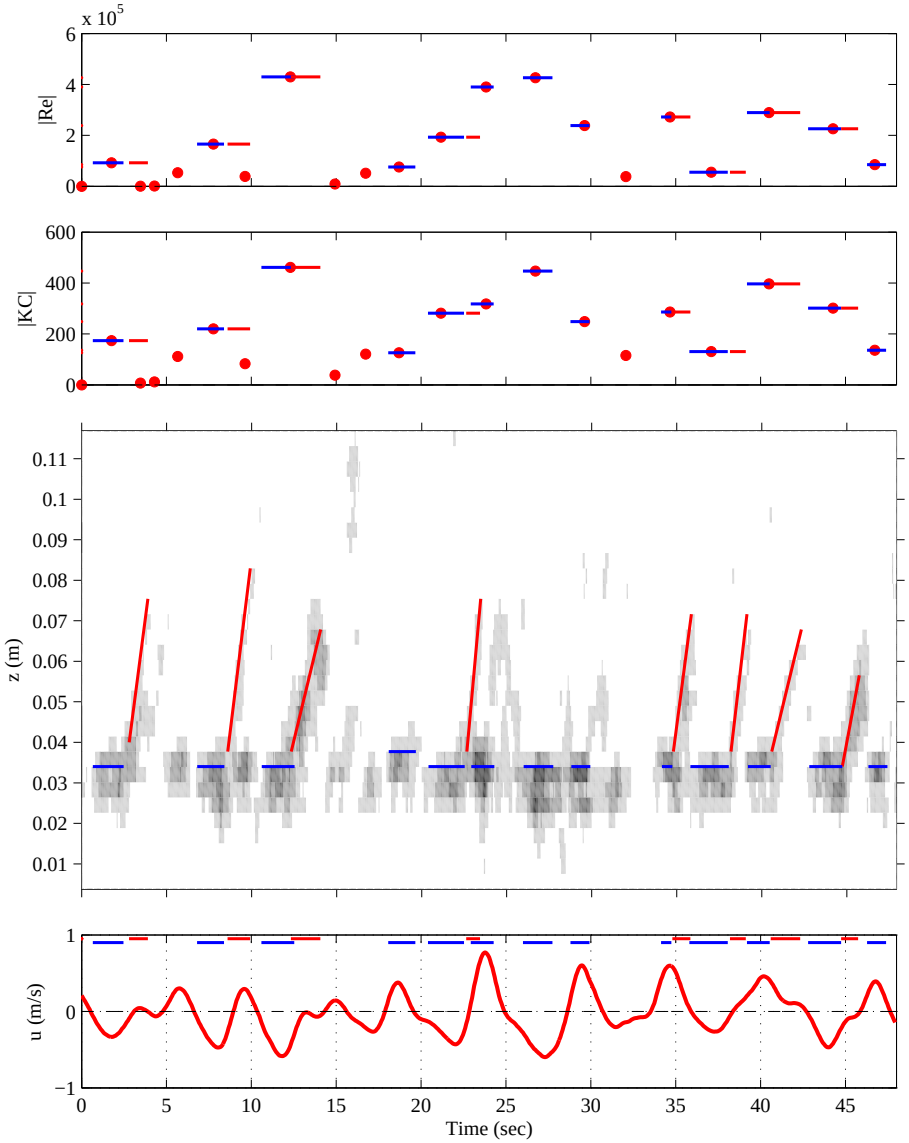

Figure 7: A time series of the ADV horizontal free stream velocity (lower panel) , the horizontally-averaged swirling strength (center panel) and the absolute value of the Reynolds number and Keulegan-Carpenter number for each $T_{1/2}$ (upper panels) for the second realization. Darker areas represent higher swirling strength. The blue and red lines superimposed on the swirling strength show occurrences of vortex generation and ejection, respectively. The blue and red lines superimposed on the velocity time series at 0.9 m/s and on the Reynolds numbers and Keulegan-Carpenter number show the temporal excursion for each of the vortex generation and ejection events, respectively.

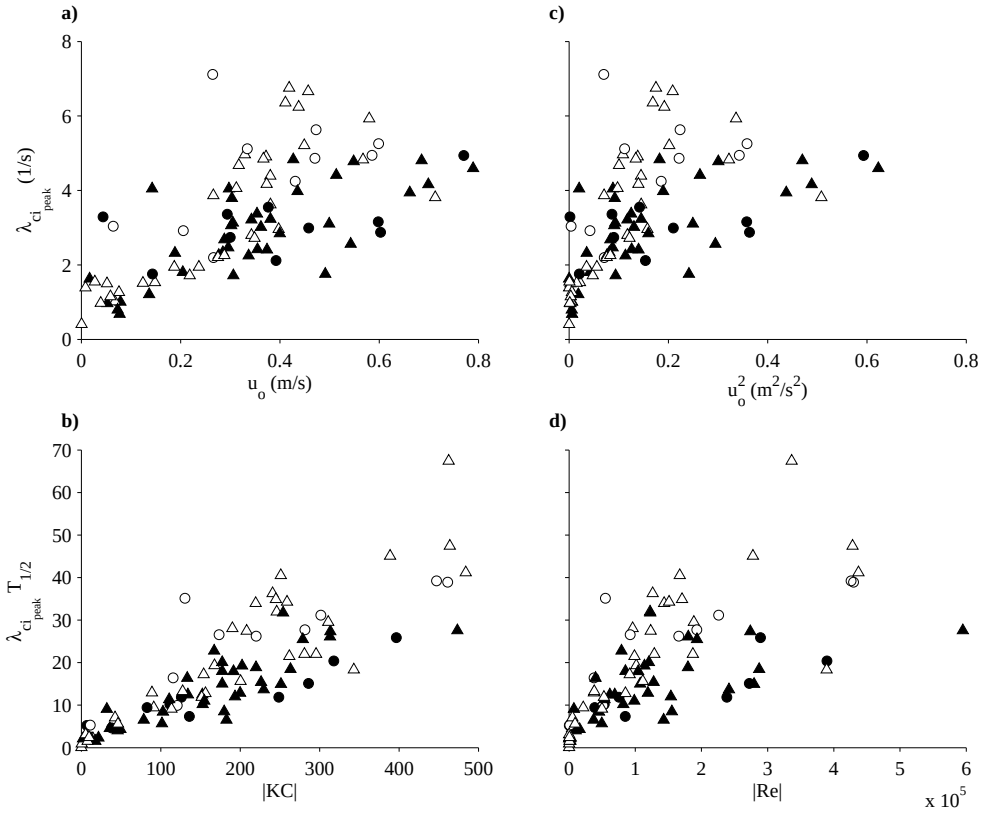

Figure 8: (upper panels) The peak swirling strength and corresponding (a) horizontal velocity or (b) horizontal velocity squared for each half wave period. (lower panels) The peak swirling strength non-dimensionalized by $T_{1/2}$ and corresponding (c) $|KC|$ or (d) $|Re|$ for each half wave period ($\circ$ = realization 2, $\triangle$ = realizations 1, 3, 4, 5). The open and filled symbols represent vortex generation events during offshore and onshore flow, respectively.